



Manganese-doped lanthanum calcium titanate as an interconnect for flat-tubular solid oxide fuel cells



Niloufar Raeis Hosseini^{a,*}, Nigel Mark Sammes^b, Jong Shik Chung^{a,b}

^aSchool of Environmental Engineering, Pohang University of Science and Technology (POSTECH), San 31, Hyoja-Dong, Nam-Gu, Pohang 790-784, Gyeongbuk, Republic of Korea

^bDepartment of Chemical Engineering, Pohang University of Science and Technology (POSTECH), San 31, Hyoja-Dong, Nam-Gu, Pohang 790-784, Republic of Korea

HIGHLIGHTS

- Manganese and lanthanum doped calcium titanate is synthesized and characterized.
- The highest electrical conductivity is 12.2 and 2.7 S cm⁻¹ in H₂ and air respectively.
- A cost effective screen-printing is developed to fabricate a dense interconnect layer.
- The maximum power density of co-sintered flat tubular cell is 207.94 mW cm⁻² at 800 °C.
- Area specific resistance of anode supported cell is 1.23 Ω cm² at 800 °C.

ARTICLE INFO

Article history:

Received 4 May 2013

Received in revised form

30 June 2013

Accepted 2 July 2013

Available online 12 July 2013

Keywords:

Flat tubular solid oxide fuel cells

Ceramic interconnect

Anode supported

Screen printing

Perovskite

ABSTRACT

A cost-effective screen-printing process is developed to fabricate a dense layer of solid oxide fuel cell (SOFC) interconnect material. A series of lanthanum–manganese-doped CaTiO₃ perovskite oxides (La_{0.4}Ca_{0.6}Ti_{1-x}Mn_xO_{3-δ}; (x = 0.0, 0.2, 0.4, 0.6)) powders is successfully synthesized using an EDTA-citrate method and co-sintered as an interconnect material on an extruded porous anode substrate in a flat-tubular solid oxide fuel cell. All samples adopt a single perovskite phase after calcination at 950 °C for 5 h. High-temperature XRD confirms that the perovskite structure is thermally stable in both oxidizing and reducing conditions. The highest electrical conductivity occurs when x = 0.6; at 12.20 S cm⁻¹ and 2.70 S cm⁻¹ under oxidizing and reducing conditions. The thermal expansion coefficient of La_{0.4}Ca_{0.6}Ti_{0.4}Mn_{0.6}O₃ is 10.76 × 10⁻⁶ K⁻¹, which closely matches that of 8 mol% yttria-stabilized zirconia. Chemical compatibility of samples and their reduction stability are verified at the operating temperature. The power density and area-specific resistance value at x = 0.6 is 208 mW cm⁻² and 1.23 Ω cm² at 800 °C under open circuit voltage, and 200 mV signal amplitude under 3% humidified hydrogen and air respectively. This performance indicates that La_{0.4}Ca_{0.6}Ti_{0.4}Mn_{0.6}O_{3-δ} has potential for use as interconnect in a flat tubular SOFC.

© 2013 Elsevier B.V. All rights reserved.

1. Introduction

Solid oxide fuel cells (SOFCs) are electrical power generators which have high power density and efficiency; they are environmentally benign due to their relatively low emission of pollutants [1,2]. SOFCs are usually designed as a series of stacks by applying an interconnect (IC) which provides a path for electricity to flow from the anode of one cell to the cathode of the adjacent one, and also excludes the fuel gas from the oxidant [3,4].

For SOFCs to be commercially viable a reliable and inexpensive IC material is required; it must have good electrical conductivity with low ohmic loss, reasonable thermal conductivity, adequate chemical and mechanical stability in both reducing and oxidizing atmospheres, similar coefficients of thermal expansion with other cell components, good sinterability, and sufficient density to prevent gas penetration [1,2].

To commercialize SOFC technology and increase cell performance, a flat-tubular (FT) SOFC has been designed; this is a combination of planar and tubular configurations. FT-SOFCs are easily sealed, tolerant of thermal stress, and have high volumetric power density. The SOFC described in this work is the anode-supported FT-SOFC, which is composed of a porous anode and a thin-coated dense membrane as an IC [5,6].

* Corresponding author. Tel.: +82 (0)54 279 4168.

E-mail address: nelirh@postech.ac.kr (N. Raeis Hosseini).

The Ceramic material is the only acceptable IC in the FT-SOFC configuration, and an alternative material to the currently-used ceramic IC (La doped-CrO₃) would be beneficial because of its difficulty in sintering to high density [7].

CaTiO₃ ceramic perovskite has attracted research attention as an appropriate material for the anode and interconnect, because of its ability to accept a variety of rare earth elements (REEs) into the titanate solid solution to make REE_xCa_{1-x}TiO₃ [8]. La³⁺ may be the most interesting REE; it converts CaTiO₃ to a n-type La_xCa_{1-x}TiO₃ semiconductor [9,10].

LaCaTiO_{3+δ} is well-known for its stability under a wide range of oxygen partial pressure (pO₂) and for high electrical conductivity, under reducing atmosphere at elevated temperature [11]. At high temperature, A-site deficient La_{1-x}Ca_xTiO₃ and La_{2(1-x)/3}Ca_xTiO₃ perovskites are n-type semiconductor ceramic oxides over a wide range of pO₂ from 10⁻¹⁵ to 10⁵ atm [12]. Lanthanum-doped SrTiO₃ (LST) has been realized as an IC material in contact with fuel gas [13], with a dense Sr_{0.7}La_{0.2}TiO₃ coated on the anode side [5]. Although LST has high electrical conductivity in a reducing environment, and is therefore suitable for use as an IC material, it undergoes phase transformation with slow redox kinetics in an oxidizing atmosphere [14]. In LST with n-type semiconducting behavior, the electrical conductivity increases after it is reduced at elevated temperature [15]. To increase the electrical conductivity and stability of LST, one suggested method is to dope it on the B-site with transitional metals (TMs) [16,17]. Partial replacement of Ti with Mn leads to a new group of lanthanum–manganese-doped SrTiO₃ perovskite oxides (LSTM) with reasonable thermal expansion, and good electrochemical activity [18,19]. Calcium has been introduced as a substitute for Sr to make LCTM perovskite oxides and different compositions has been synthesized and characterized in terms of crystal structure, thermal expansion, and transport properties (e.g., Ca_{0.67}La_{0.33}Mn_{0.33}Ti_{0.67}O₃, La_{0.1}Ca_{0.9}Mn_{1-x}Ti_xO₃, and La_{0.5}Ca_{0.5}Mn_{0.5}Ti_{0.5}O₃) [11,20,21]. However, until now, systematic investigation of Mn substitution effect on La doped calcium titanates under both oxidizing and reducing conditions has not been done. The current work has been conducted to evaluate the feasibility of using LCTM for construction of ICs in FT-SOFC stacks. In this work, we undertake a detailed study of the crystal structure, microstructure, sintering behavior, thermal expansion, electrical conductivity, reduction stability, and polarization behavior to show that the compound is a potential candidate for use as a dense IC film on an anode-supported SOFC.

2. Experimental

2.1. Preparation of interconnect powder

A series of La_{0.4}Ca_{0.6}Ti_(1-x)Mn_xO_{3-δ} (x = 0.0, 0.2, 0.4, 0.6) perovskite powders (hereafter abbreviated as LCTMx, 0 ≤ x ≤ 0.6) was

prepared using a modified EDTA-citrate method [22]. Calculated amounts of La(NO₃)₃·6H₂O (99%, Aldrich), Ca(NO₃)₂·4H₂O (98.50%, Aldrich), Mn(NO₃)₂·6H₂O (98%, Aldrich) and Ti(OCH(CH₃)₂)₄ (97%, Aldrich) solution in ethanol (97%, Aldrich), were dissolved in EDTA (99.9%, Aldrich)–NH₄OH (28%, Daejung) buffer solution. The molar ratio of EDTA:total metal ion:citric acid was held at 1:1:1.5 under constant stirring.

The mixture was heated to 80 °C; a gel resulted, which was then dried at 150 °C overnight in an oven in air to yield a black powder. To remove all carbon remnants, the powder was pre-calcined at 700 °C for 1 h. The resulting powder was homogenized by ball-milling with zirconia balls for 12 h. The fine reactive LCTMx powders produced by grinding were then calcined at 950 °C for 5 h. Alpha-terpinol (Aldrich) and ethyl cellulose (Aldrich) were mixed in a ratio of 90:10 w:w and then stirred for 24 h at 80 °C as a paste for IC screen printing.

2.2. Flat tubular cell fabrication

The anode support was fabricated by extrusion of a mixture of NiO (JT Baker) and 8 mol% Y₂O₃-stabilized zirconia (YSZ) (Tosho) in a ratio of 55:45 w:w which had previously been ball milled at 80 rpm for 4 days. After drying at 80 °C for 24 h the mixture was fired at 900 °C for 6 h. Polyvinyl butyral (PVB) as an organic binder, and 10 wt% graphite (Aldrich) as a pore former, were added to the NiO–YSZ mixture and it was allowed to age for 1 day, followed by a repeat of the mixing and firing processes. The mixture was then extruded through a die, using an extruder (KSM 5A, Electro Chuk-Master). The resultant flat tube was 280 mm long, 28 mm wide, 5 mm thick and included five rectangular holes (Fig. 1).

This extruded anode support was pre-sintered at 1200 °C for 3 h, then dipped into a slurry of anode functional layer (AFL) with the same components such that the ratio of NiO:YSZ was kept at 55:45 w:w, and sintered in air at 900 °C for 3 h. The obtained thickness of the AFL was 10 μm. A rectangular area of anode support (2 × 16 cm = 32 cm²) on one side was masked for interconnect coating, and YSZ slurry was dip-coated as an electrolyte and sintered at 900 °C for 3 h to achieve a thickness of 15.9 μm. The synthesized LCTMx was milled using an attrition mill (KMDC-0.5B) for 6 h, sieved through a 325-μm mesh then mixed with Alpha-terpinol/ethyl cellulose paste using a mortar and pestle. The dense LCTMx powder was coated as a 20-μm thin film on the YSZ-uncoated area of anode support using screen-printing. The anode support, AFL and IC were co-fired at 1400 °C for 3 h to obtain a half-cell. The full cell was obtained by forming two cathode layers of (La_{0.85}Sr_{0.15})_{0.9}MnO₃–YSZ composite (LSM–YSZ) and (La_{0.85}Sr_{0.15})_{0.9}MnO₃ (LSM) on the other side of the anode support using spray-gun coating and sintering at 1200 °C for 3 h. Finally, a spray-gun was used to coat slurry of La_{0.6}Sr_{0.4}Co_{0.2}Fe_{0.8}O₃ (LSCF) on the sintered cathode layers as a

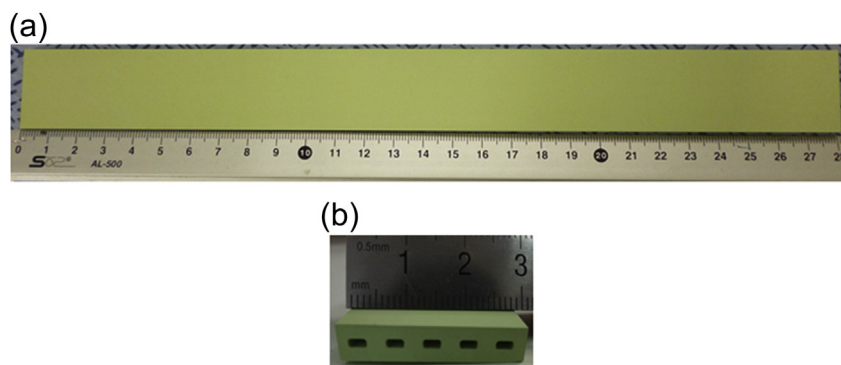


Fig. 1. (a) Photograph of fabricated flat tubular anode support, and (b) Cross section of the extruded anode support.

current-collecting layer. The three layers of the cathode side were sintered at 1100 °C for 3 h, and their areas were kept at 30 cm².

2.3. Powder characterization

To determine the calcination temperature, thermogravimetric analysis (TGA) and differential thermal analysis (DTA) were conducted using a thermal analyzer (Labsys–Calisto) from room temperature to 1000 °C at 5 °C min^{−1}. Rectangular bar specimens (2 mm × 6 mm × 15 mm) were cold pressed iso-statically using a uniaxial force at 200 MPa, and then sintered at 1400 °C for 10 h in air.

Phase analysis of the powders and sintered bars was conducted using room-temperature X-ray diffraction (RT-XRD) analysis on a Rigaku diffractometer using Cu–K α radiation ($\lambda = 1.5418$ Å) at 40 kV and 100 mA. For lattice expansion studies, the in-situ high-temperature XRD (HT-XRD) patterns of LCTMx calcined powders were recorded from room temperature up to 1000 °C in air and 4% H₂–Ar, on a Philips X'pert Pro-MPD X-ray diffractometer with secondary beam graphite monochromated Cu–K α radiation. The scanning range for 2θ was 20°–80° in increments of 0.02° for both RT-XRD and HT-XRD; related lattice parameters of samples were calculated by Rietveld refinement using MDI Jade9 software. The relative densities of the samples were measured using standard Archimedes tests.

The microstructures of the powders, sintered bars and cross-section of interconnect film on the anode support were observed visually using a scanning electron microscope (SEM) (High Resolution FE-SEM/EDX, JEOL JSM-7401F). Specimens were cut, then fine-polished to 1200 μ m and thermally etched at 1375 °C for 30 min at 5 °C min^{−1}. Before imaging, samples were sputtered and silver coated in Ar gas for 45 s using a Cressington sputter coater. Sintering behavior of the specimens, including thermal expansion (TE) and sintering shrinkage, was measured on sintered bars using a dilatometer (Netzsch, DIL 402 PC) at 30–1000 °C and 1400 °C at heating and cooling rates of 5 °C min^{−1} and 10 °C min^{−1}, respectively.

Temperature-dependent electrical conductivity was measured by a standard four-probe dc technique using a multi-meter (Model 2000, Keithley Inc.) in both air and a mixture of 5% H₂ in Ar.

The chemical states of Mn and Ti of LCTMx was obtained from X-ray Photoelectron Spectroscopy (XPS) measurements (VG Scientific, ESCALAB 220iXL) using Mg K α radiation (1253.6 eV) at room temperature. The binding energy calibration was performed using C1s peak in the background as the reference energy.

The chemical stability of calcined powders was examined using XRD after annealing at elevated temperature (900 °C) in humidified 5% H₂–Ar for 100 h.

Chemical compatibility of LCTMx with the anode and cathode cells was examined by mixing the powders with 8 mol% YSZ–NiO and LSM powder in a weight ratio of 50:50, ball-milling for 1 day, sintering at 1400 °C for 20 h and then analyzing using XRD.

2.4. Unit cell characterization

Performance of the unit cell, with the four-electrode configuration, was measured using an electronic loader (Nextech, EI-300P) between 700 °C and 800 °C. The unit cell was mounted on a fuel cell station and platinum meshes were attached with gold wires to the surface of the cathode and interconnect layers using LSCF paste as a current collector (Fig. 2). Electrochemical impedance spectra (EIS) was measured using multi-channel potentiostat (Biologic, SP300), with 200 mV signal amplitude, under open circuit voltage (OCV) and 3% humidified hydrogen was fed to the anode while air was fed to the cathode with a flow of 500 and 1000 mL min^{−1} respectively.

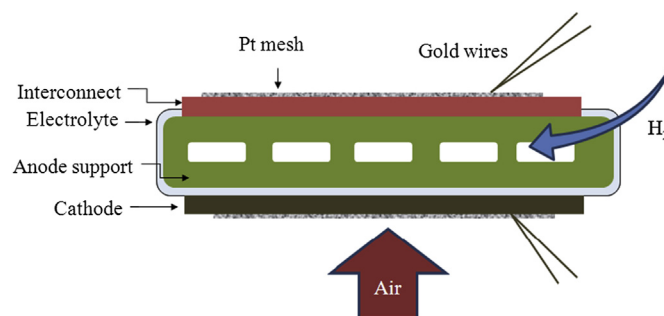


Fig. 2. Schematic diagram of anode-supported flat-tubular solid oxide fuel cell.

3. Results and discussion

To study the calcination temperature and profile of the samples, dried LCTM0.0 gel was analyzed using TGA (Fig. 3). Based on the TGA curve, a 5% weight loss took place at 190.8 °C. An exothermic DTA peak at 342.15 °C with 10% weight loss confirmed the absorbed and hydrated water loss. At temperature around 500 °C, decomposition of the nitrates led to 80% loss of weight accompanied by an endothermic peak at 420 °C. However, all of the organics combusted at approximately 500 °C, thus the pre-calcination was performed at 700 °C to ensure total reaction (Fig. 3). RT-XRD patterns of the LCTMx samples, after calcination at 950 °C for 5 h, exhibited the formation of a well-crystallized single-phase orthorhombic perovskite structure of the space group *Pbnm*. (Fig. 4a). The maximum XRD peaks (Fig. 4b) all shifted to lower angles due to an increase of the lattice parameters, although LCTM0.6 showed a relatively small shift. An increase in the lattice constant has been explained by substitution of Mn³⁺ at Ti⁴⁺ sites in the lattice accompanied by radius differences at $x \leq 0.4$. However, in LCTM0.6, oxygen vacancies are created and Mn valence is increased to Mn⁴⁺ [18]. Further Mn doping leads to a small decrease in lattice volume at 60 mol% because Mn has a smaller ionic radius than does Ti [18]. It may be ascribed to random distribution of Mn on the B-site according to Vegard's law [19] (Fig. 4c). The phase stability of LCTMx was confirmed using XRD after annealing in 5% H₂–Ar for 100 h in a reducing environment. Because LCT is stable under reducing conditions, there was no secondary phase in the XRD peaks. The absence of additional diffraction peaks in the XRD pattern for the annealed samples indicates that no secondary phases formed; thus LCTMx is cyclically stable (Fig. 5).

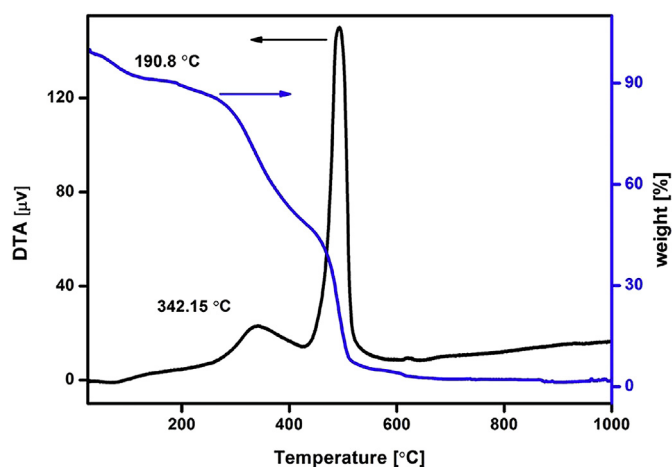


Fig. 3. TG-DTA curves of LCTM0.0 gel dried at 150 °C for 8 h.

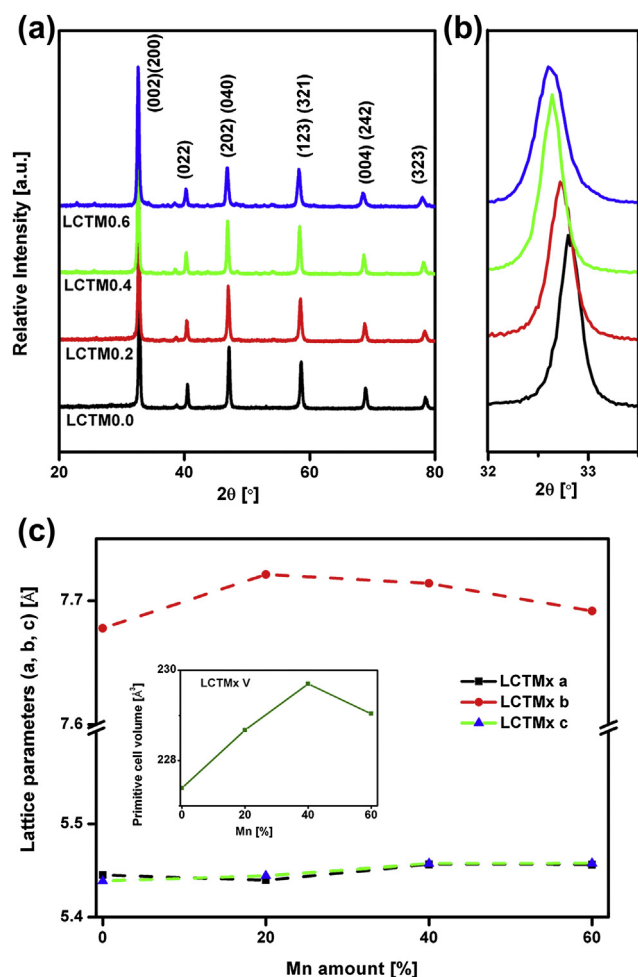


Fig. 4. (a) Room temperature XRD patterns of LCTMx ($0 \leq x \leq 0.6$) oxides after calcination in air, (b) magnified peak positions, and (c) lattice parameters of LCTMx ($0 \leq x \leq 0.6$) according to different amounts of Mn doping.

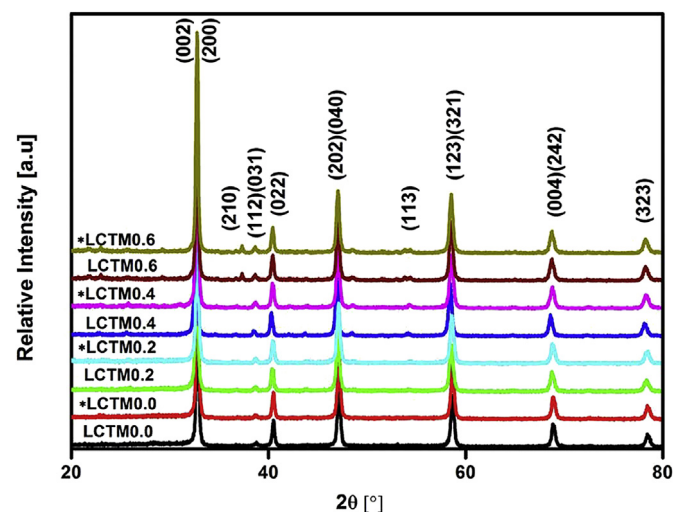


Fig. 5. XRD patterns of LCTMx ($0 \leq x \leq 0.6$) after annealing in humidified 5% H_2 –Ar (*LCTMx) at 900 °C for 100 h.

Phase analysis was conducted, using HT-XRD while heating the calcined powders from room temperature to 1000 °C under air and 4% H_2 –Ar. LCTM0.6 was analyzed and confirmed to be thermally stable under both oxidizing and reducing conditions (Fig. 6a–d). The lattice parameters evolution for LCTM0.6 upon increasing temperature from room temperature to 1000 °C under air and 4% H_2 –Ar, shows that the unit cells expanded more under reducing conditions compared to oxidizing conditions (Fig. 7).

SEM micrographs of the sintered specimen at 1400 °C for 10 h with a theoretical density $\geq 96\%$, confirmed a well-sintered material and well-defined grains (Fig. 8). An SEM micrograph of co-sintered LCTMx and porous anode support cross section shows a dense IC with a thickness of approximately 20 μm ; it also confirms that the IC adhered well to the anode during the co-firing process (Fig. 9a, b).

To characterize the shrinkage behavior, starting and ending temperatures of sintering are important factors. They indicate agglomeration and densification temperatures which are depicted from sintering shrinkage graph (Fig. 10). Moreover, sintering behavior between 500 °C and 1400 °C shows a slow shrinkage over a wide range of temperature. The effect of Mn doping on sintering shrinkage ($\Delta L/L_0$, where ΔL is change in length and L_0 is initial length) indicates that un-doped LCTM0.0 started to shrink at 1050 °C and that shrinkage was 2.7% at 1215 °C, whereas LCTM0.2 shrank at temperatures between 1045 °C and 1285 °C; this behavior may be due to formation of secondary phases during sintering (Fig. 10). Adding >20 mol% Mn reduced the sintering temperature to slightly less than 1010 °C. Acceptor–donor doped

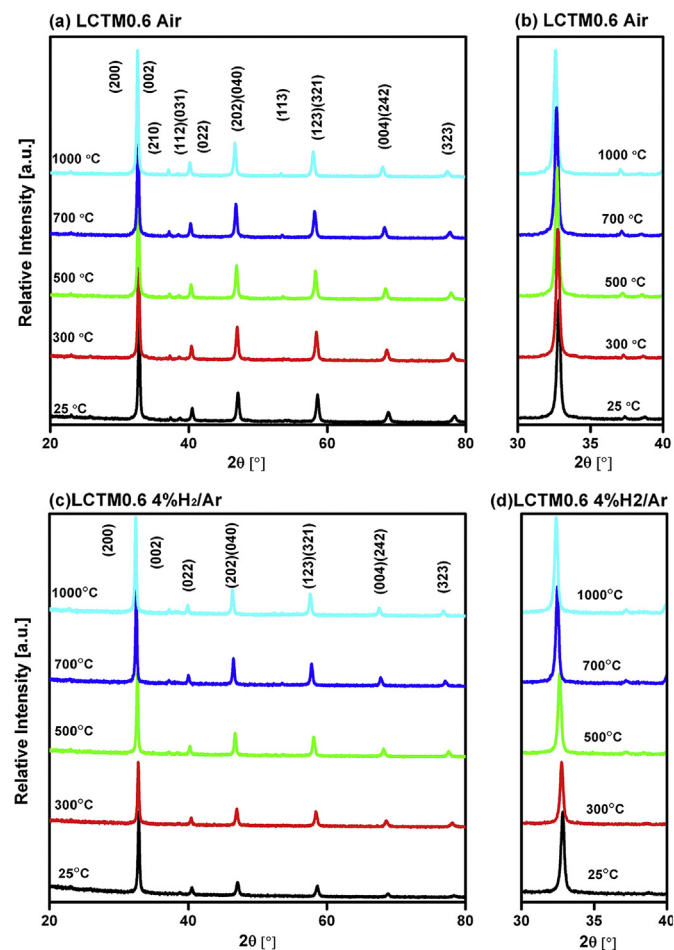


Fig. 6. (a, b) High-temperature XRD patterns of LCTM0.6 oxides from room temperature to 1000 °C under air and (c, d) under 4% H_2 –Ar.

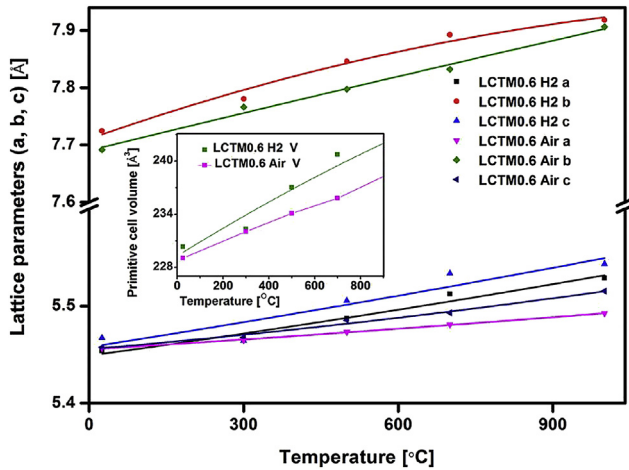


Fig. 7. Thermal evolution of refined lattice parameter of LCTMx ($x = 0.6$) under heating in air, and 4% H_2 -Ar.

$CaTiO_3$ materials do not have inferior sintering behavior as chromates do; so more than 20 mol% Mn doping improved sintering properties slightly. The temperature-dependent shrinkage rate ($d(\Delta L/L_0)/dT$) can be used to determine the optimum sintering temperature for LCTMx.

Inflection in sintering curves is generally ascribed to a change in sintering mechanism as an evidence of liquid phase generation [2]. However, to explicate the exact sintering mechanism in LCTMx ceramic perovskites, further studies are required.

Electrical conductivity is influenced by the microstructure of samples according to sintering conditions [23]. Electrical conductivity of air-sintered samples was measured separately under air and under moist 5% H_2 -Ar as oxidizing and reducing environments respectively. The dependence of electrical conductivity of LCTMx on temperature in air was measured at 50-°C intervals during cooling of samples from 900 °C, after holding them for ≥ 5 h at each temperature to reach equilibrium. The conductivity relationship can be given by:

$$\sigma = \frac{A}{T} \exp\left(-\frac{E_a}{KT}\right) = e\mu_n n + e\mu_p p + ez_i [i]; \quad (1)$$

where A is a constant, T is absolute temperature, E_a is the activation energy, K is the Boltzmann constant, e is the elementary charge, μ is the carrier mobility, z_i is the ion charge, n is the electron concentration, p is the hole concentration, and $[i]$ is the ion concentration [24]. LCTM0.0 showed very low electrical conductivity in air especially at $T < 700$ °C; thus in this work it was only studied from 700 °C to 1000 °C. In the undoped sample (LCTM0.0) under oxidizing conditions, because of high pO_2 the extra oxygen in the lattice causes a rearrangement of the structure to pyrochlore $La_2Ti_2O_7$, and it is satisfied by Ca vacancy (V''_{Ca}) [17]; in this structure, V''_{Ca} rather than electron hopping, is responsible for electrical conductivity. The absence of oxygen vacancies and Ti'_{Ti} as ionic and electronic charge carriers respectively makes the material very poor electronic conductor, but under reducing conditions, there is no extra oxygen to enter the lattice and Ti'_{Ti} increases; thus the compound's electrical conductivity increases [18].

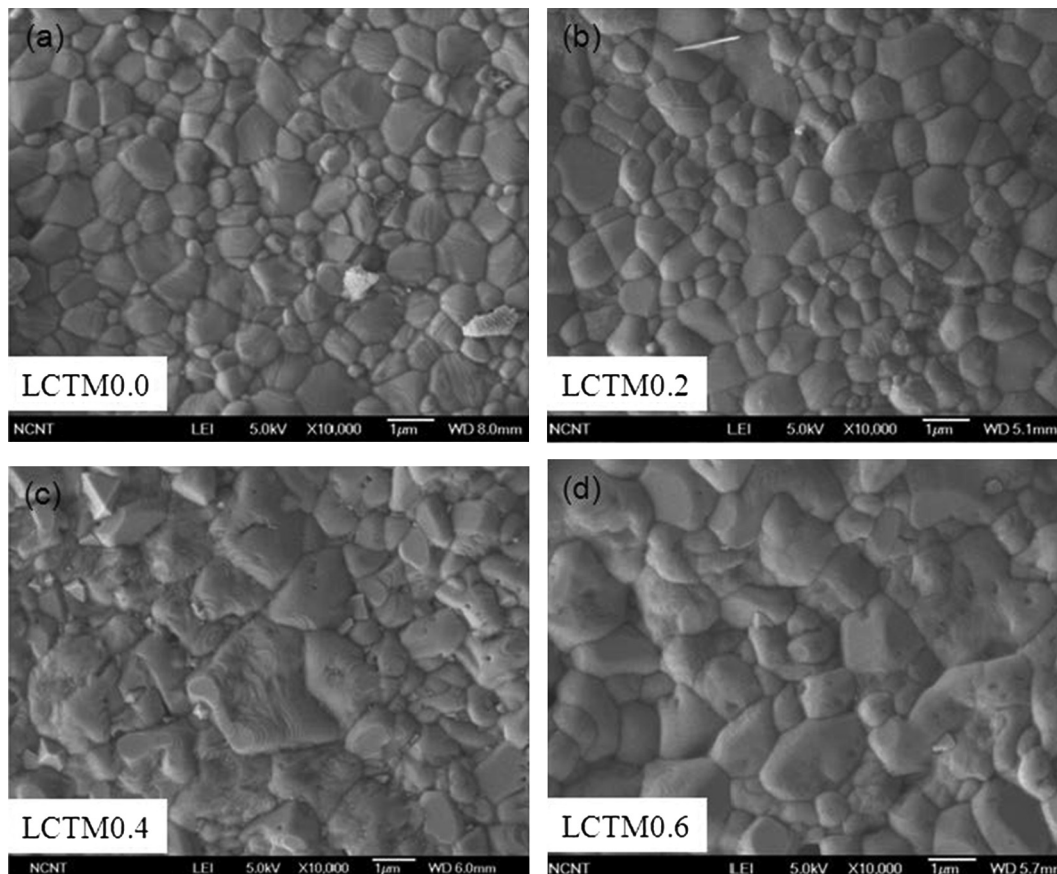


Fig. 8. SEM micrograph of LCTMx ($0 \leq x \leq 0.6$) specimens, sintered at 1400 °C for 10 h thermal etched at 1375 °C.

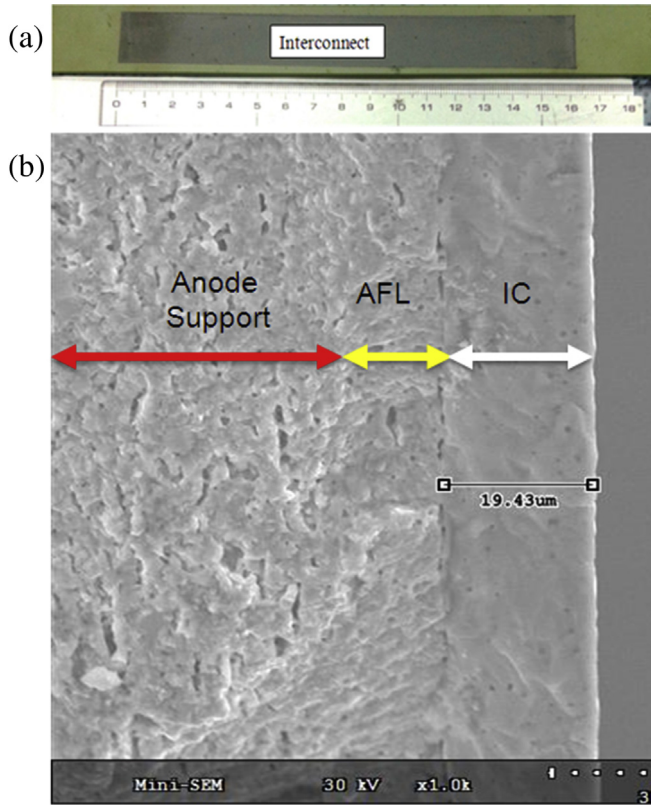


Fig. 9. (a) Anode-supported flat tubular SOFC with a dense interconnect membrane, and (b) SEM images of anode support and cross-section of the interconnect membrane on the anode support.

Increasing Mn content decreased E_a and increased electrical conductivity in air; E_a in air was $180.8 \text{ kJ mol}^{-1}$ in LCTM0.0, but $45.38 \text{ kJ mol}^{-1}$ in LCTM0.2. Mn doping also caused an increase in total electrical conductivity of the samples from $1.47 \times 10^{-4} \text{ S cm}^{-1}$ in LCTM0.0 to $\sim 1.32 \text{ S cm}^{-1}$ in LCTM0.2 (Fig. 11a). Mn^{3+} doping causes an acceptor-type defect which leads to an improvement in conductivity at p-type region (Eq. (2)). It can be written in Kroger–Vink [25] notation as:

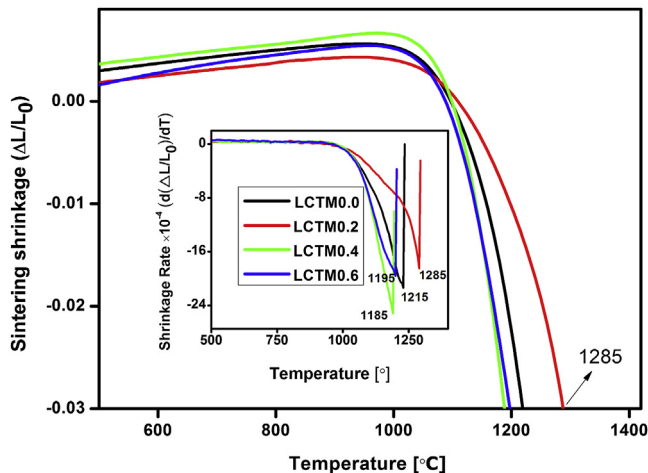
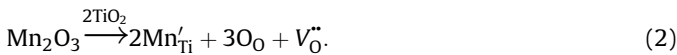


Fig. 10. Sintering behavior ($\Delta L/L_0$) of LCTMx; and (inset) shrinkage rate ($d(\Delta L/L_0)/dT$) as a function of temperature between 500 °C and 1400 °C.

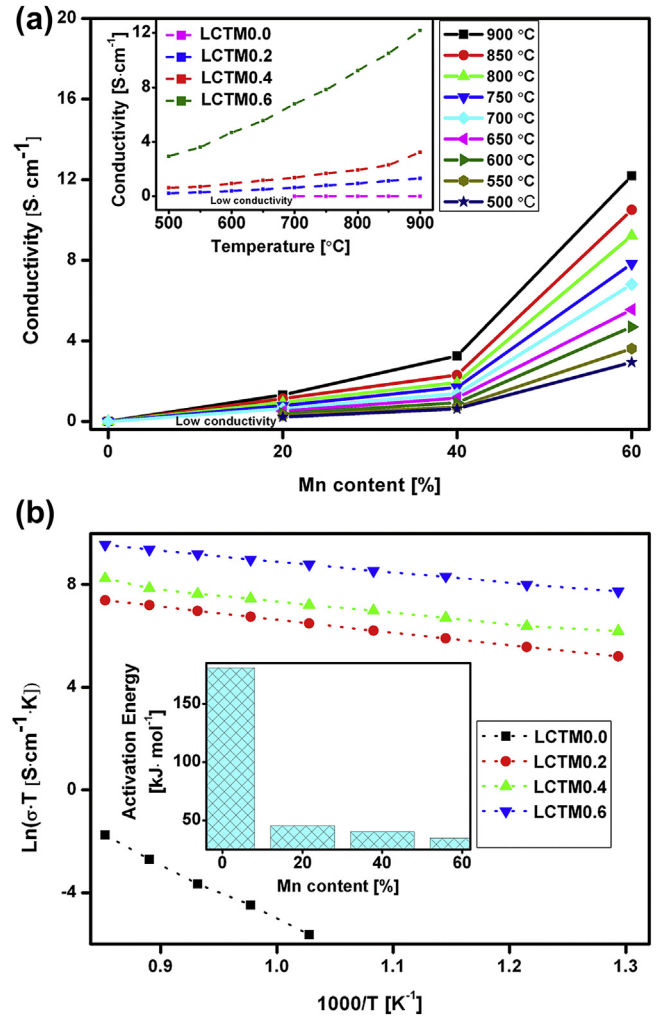


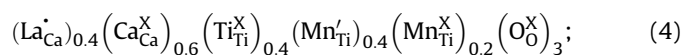
Fig. 11. (a) Effect of Mn-doping on temperature dependent electrical conductivity of LCTMx ($0 \leq x \leq 0.6$); (inset) temperature dependence of electrical conductivity of LCTMx ($0 \leq x \leq 0.6$) under air, and (b) Arrhenius plot for LCTMx ($0 \leq x \leq 0.6$); (inset) effect of Mn-doping on activation energy of LCTMx ($0 \leq x \leq 0.6$) under air.

Increasing Mn content causes the number of oxygen vacancies to increase and this in turn causes an increase in electron hole concentration (Eq. (3)).



This phenomenon results in high conductivity under oxidizing conditions [26].

The log–linear relationship between σT and $1/T$ (Fig. 11b) indicates that the conductivity behavior obeys the small-polaron hopping mechanism. In LCTM0.6 under oxidizing conditions, Mn^{4+} is responsible for the compensation mechanism and the compound could be shown as Eq. (4);

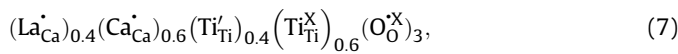
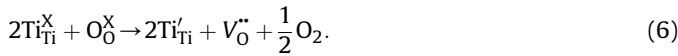


where



The high electrical conductivity of LCTM0.6 ($\sim 12.2 \text{ S cm}^{-1}$) has been ascribed to the presence of Mn^{4+} , which may changes the conduction mechanism from small-polaron hopping to broad-band

conduction, which requires less energy than polaron hopping to mobilize electron charge carriers [14,18]. Before measuring electrical conductivity in humidified 5% H₂–Ar, samples were stabilized by holding them at 900 °C for 20 h. The cooling step intervals from high temperature were 50 °C, as in the air condition. Under reducing conditions the electrical conductivity of LCTM0.0 reached 2.38 S cm⁻¹ (Fig. 12a) which has been explained as the n-type behavior of undoped sample under wide range of oxygen partial pressure [18]. In La_{1-x}Ca_xTiO_{3-d} system, reduction of Ti⁴⁺ to Ti³⁺ makes oxygen leave the lattice and creates a defect that causes n-type conductivity [11] (Eq. (6,7))



in which the formation of oxygen vacancies can be ignored, so the compensation mechanism is

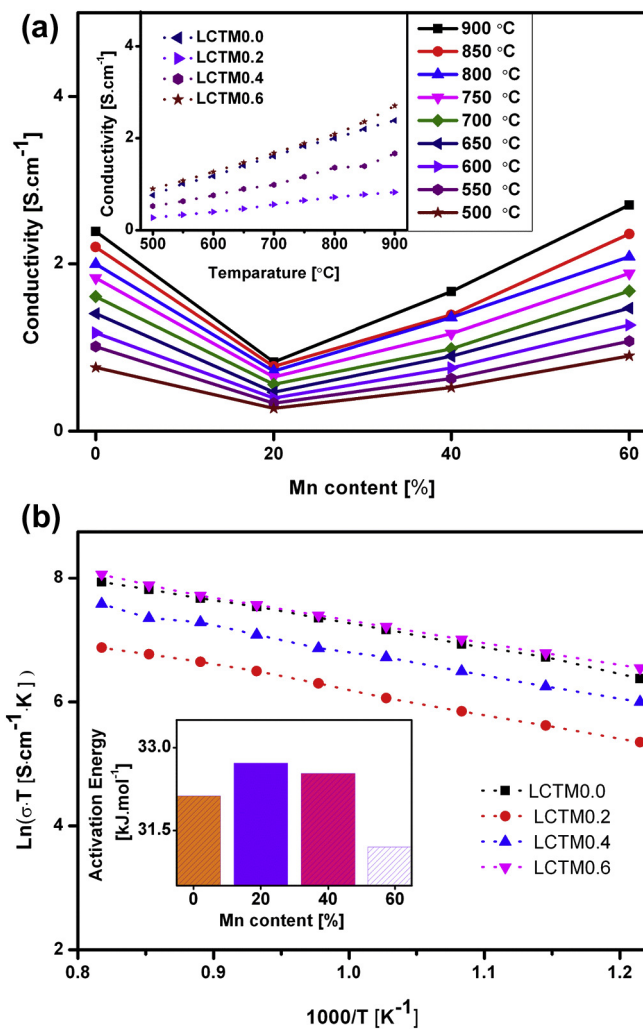
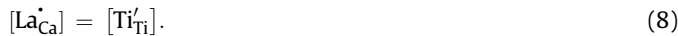


Fig. 12. (a) Effect of Mn-doping on temperature dependent electrical conductivity of LCTMx ($0 \leq x \leq 0.6$); (inset) temperature dependence of electrical conductivity of LCTMx ($0 \leq x \leq 0.6$) under humidified 5% H₂–Ar, (b) Arrhenius plot for LCTMx ($0 \leq x \leq 0.6$) under humidified 5% H₂–Ar.

While under extremely reducing conditions, the number of oxygen vacancies is not negligible; they cause an increase in Ti³⁺ ions [18]:



The temperature dependence of electrical conductivity under reducing conditions increased with increasing Mn content, except LCTM0.0, which electrical conductivity is higher in LCTM0.0 than that of LCTM0.4 (Fig. 12a). It has been postulated that this is due to Mn²⁺ acceptor doping at $x = 0.2, 0.4$ which causes a decrease in free electron concentration compare to that in un-doped LCTM [27]. The maximum electrical conductivity was 2.70 S cm⁻¹ for LCTM0.6 (Fig. 12a); it has been explained by the existence of Mn⁴⁺ cations which cause ease of reduction by Mn_{Ti}^X and release more oxygen than other compositions [18]. The Arrhenius plot (Fig. 12b) of LCTMx conductivity under reducing conditions shows that it follows the small-polaron hopping mechanism. The reasonable electrical conductivity of LCTM0.6 in a dual atmosphere led us to coat it as an IC layer on the anode substrate and test the performance in an anode-supported FT-SOFC cell.

XPS survey spectrum peaks of LCTM0.6 show that the particles contain elements of Ti, Ca, O, and La, Mn, and a trace amount of carbon. The binding energies of Ti2p_{3/2}, Mn2p_{3/2}, O1s, Ca2p, and La3d_{5/2} are 454, 639, 531, 347, and 836 eV respectively (Fig. 13a). The achieved XPS spectra of Mn2p represent a broad peak of 2p_{3/2} separated into two peaks at 641.78 and 643.49 eV related to Mn₂O₃ and MnO₂. It was followed by another peak of 2p_{1/2} postulate to MnO₂. It illustrates that Mn element corresponds to Mn⁴⁺ and Mn³⁺ in LCTM0.6 (Fig. 13b). The detailed XPS spectra of Ti2p_{3/2} show that Ti peak is positioned at 458.87 eV. This binding energy is in good match with chemical state for CaTiO₃ and TiO₂. The Ti element corresponds to Ti⁴⁺ (Fig. 13c). It proves that the solid solution obeys Eq. (4) which supports the defect model of LCTM0.6.

Thermal stress, which leads to performance degradation and SOFC failure, is common in fabrication and thermal cycles, so all components should have similar thermal expansion coefficients (TECs) [28]. The average expansion coefficient for temperature T is defined by Eq. (10):

$$\text{TEC} = \frac{1}{L_0} \left(\frac{\partial L}{\partial T} \right); \quad (10)$$

where L_0 and L are the length of sample at room temperature and under heating respectively. TEC can be estimated as the cube root of lattice volume obtained from the lattice parameters by Eq. (11) [2].

$$\sqrt[3]{\alpha} = \sqrt[3]{\frac{1}{V_0} \left(\frac{\partial V}{\partial T} \right)} = \frac{1}{L_0} \left(\frac{\partial L}{\partial T} \right). \quad (11)$$

The thermal expansion of LCTMx is closely matched with that of 8-mol% YSZ ($10.6 \times 10^{-6} \text{ K}^{-1}$) at temperatures between 25 °C and 1000 °C (Fig. 14). The calculated TEC of LCTM0.0 was $10.68 \times 10^{-6} \text{ K}^{-1}$, which is similar to the TEC of YSZ. The TEC of LCTM0.2 was $11.63 \times 10^{-6} \text{ K}^{-1}$, slightly higher than that of LCTM0.0 but still close to that of YSZ. However increasing the Mn content decreased the TEC of LCTMx to a minimum of $10.76 \times 10^{-6} \text{ K}^{-1}$ for LCTM0.6. This decrease can be ascribed to differences in ionic radii of Mn and Ti ions and is in good agreement with HT-XRD results and obtained lattice parameters. Thus, the TEC of LCTM appears to be controlled by Mn doping at Ti sites.

To confirm the compatibility of the interconnect with the anode and electrolyte, a 50:50 wt% mixture of LCTMx powder and NiO – 8 mol% YSZ was ball milled, dried, and co-sintered at 1400 °C for 30 h (Fig. 15a). The same process was applied for LSM as the

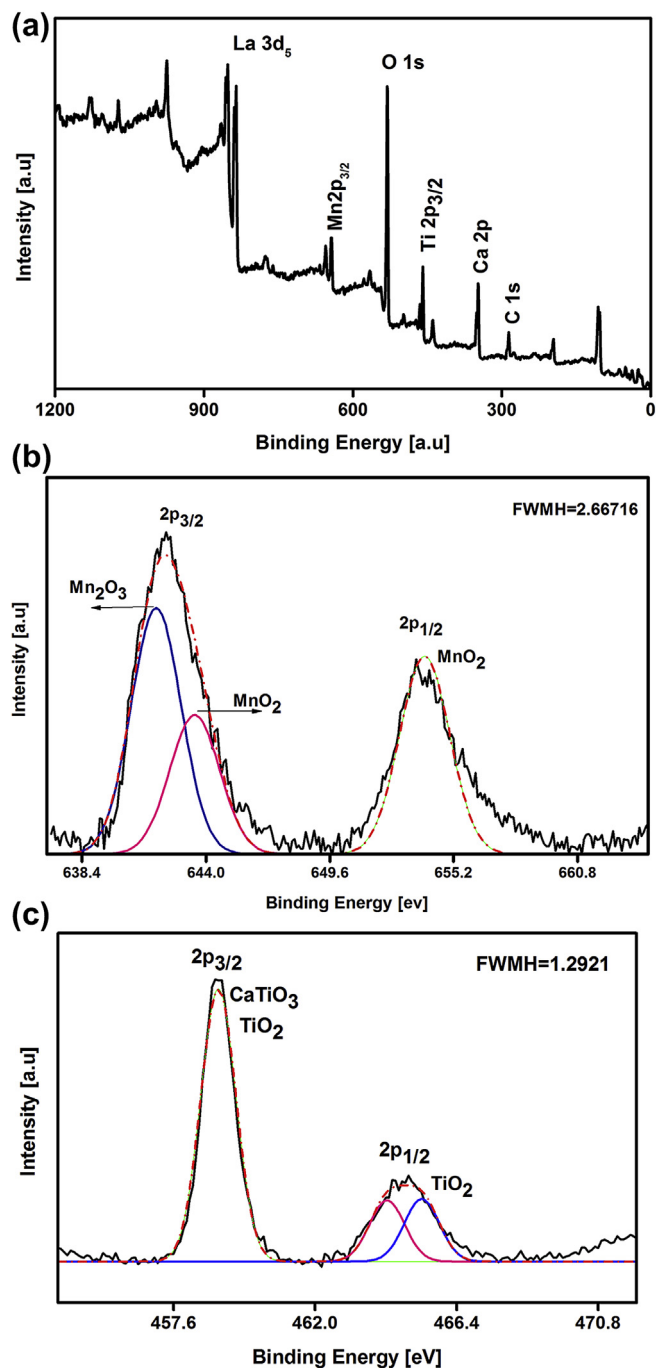


Fig. 13. (a) XPS survey spectrum of the typical 60 mol% Mn-doped LCTMx, (b) Fitted XPS spectra of the Mn2p level of LCTM0.6, and (c) Fitted XPS spectra of the Ti2p level of LCTM0.6.

cathode material, except that the sintering temperature was 1200 °C for 30 h (Fig. 15b). According to the observed XRD peaks, no significant secondary phase formation occurred, so no reaction should occur between the interconnect and other cell components under normal conditions of SOFC sintering and operation. The absence of additional diffraction peaks in the XRD pattern for the annealed samples indicates that no secondary phases formed; thus LCTMx is a cyclically stable material.

It is worth to mention that co-sintering during FT-cell fabrication leads to creation of triple phase boundaries (TPBs) providing sites for charge-transfer reaction [29]. Moreover the long sintering

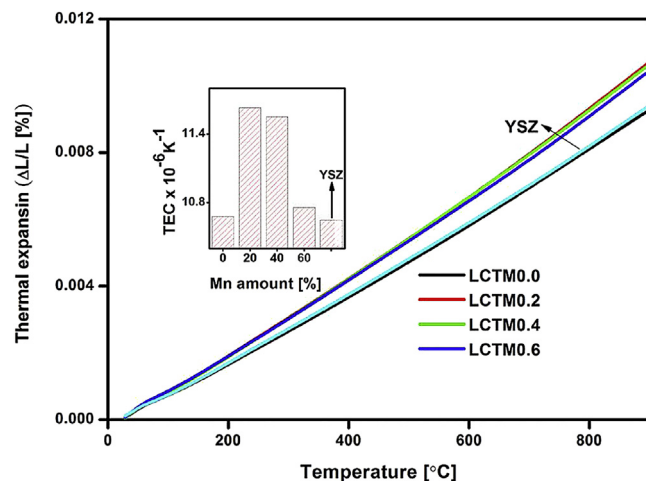


Fig. 14. Linear isothermal expansion as a function of temperature; and (inset) thermal expansion coefficient (TEC) for LCTMx ($0 \leq x \leq 0.6$).

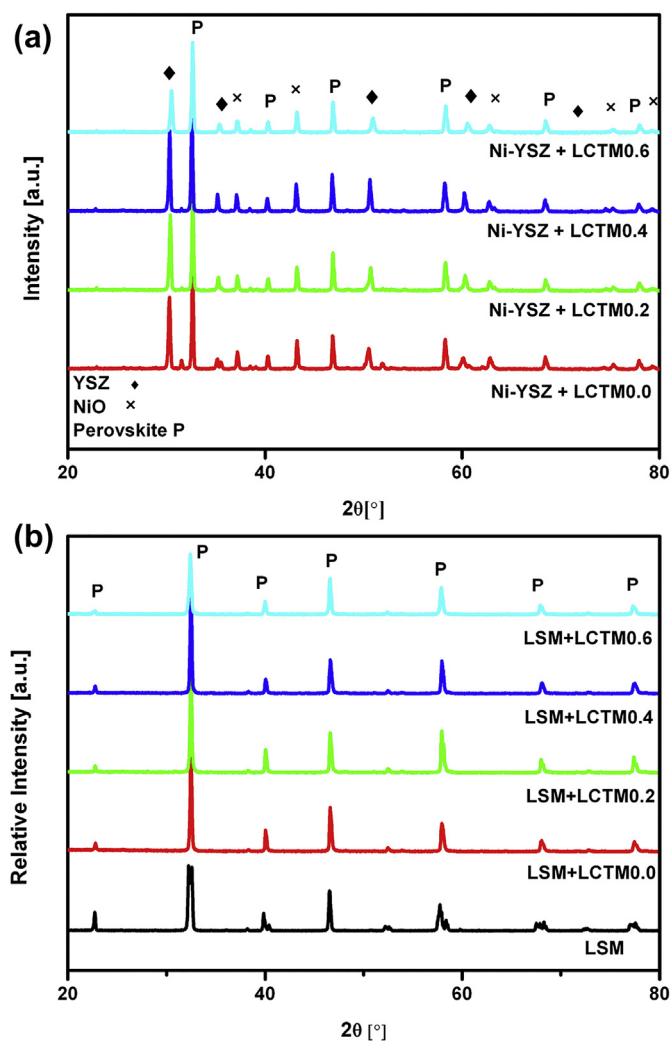


Fig. 15. (a) XRD patterns of mixture of LCTMx and 8 mol% YSZ and NiO (50:50 wt%) fired at 1400 °C for 30 h, and (b) mixture of LCTMx and LSM (50:50 wt%) fired at 1400 °C for 30 h.

time leads to a reduction in TPB length. To avoid this phenomenon by long sintering period, it is necessary to carefully control the time in an optimal range.

To assess the electrochemical performance of the anode-supported FT-SOFC, impedance analysis measurements were conducted in the frequency range from 1×10^3 Hz to 1×10^{-2} Hz under open circuit voltage (OCV). Area specific resistance (ASR) values of the FT-single cell with LCTM0.6 IC were determined from the amplitude of the Nyquist plot (Fig. 16) between 700 °C and 800 °C. The calculated ASRs were $1.23 \Omega \text{ cm}^2$ at 800 °C, $1.44 \Omega \text{ cm}^2$ at 750 °C and $2.04 \Omega \text{ cm}^2$ at 700 °C. As expected, ASR increased as temperature decreased. According to Nyquist plot, the intercept of the impedance arcs with the real axis at high frequencies is ascribed to the ohmic resistance (R_{ohm}) which is equal to $0.7284 \Omega \text{ cm}^2$ (Fig. 16).

ASR value is in a direct relation with thickness of electrolyte, anode support and cathode interlayer; whereas, increasing porosity of anode support leads to a decrease in ASR [30].

One of the parameters affecting ASR to be relatively high is concentration polarization. The high ASR indicates that diffusion condition is inappropriate due to improper amount of pore former to produce optimized pores to the electrode. Therefore an increase in ohmic resistance is ascribed to pore-former amount which plays a significant role in deteriorating the R_{ohm} [31].

A weak lateral and transverse conduction through the electrode layer leads to diffusivity of electron transfer at TPB and consequently large polarization and ohmic resistance.

High R_{ohm} arises from the electron-transfer and ion-transfer processes because of improper contact between electrode–current collector, and electrode–electrolyte interfaces [32,33]. Reduced ionic conduction through electrolyte is responsible for elevated ohmic resistance, because ionic conductivity of electrolyte governs the ohmic resistance.

Another affecting parameter is non-uniform electrolyte thickness during dip coating process. In results, a rapid deterioration occurs in thinner areas of electrolyte due to producing small pinholes of electrolyte through discontinuous geometric contact at the interfaces [30–33].

The variation of cell voltage and power density as a function of current density for the anode-supported FT-cell coated with LCTMx as an IC in the temperature range of 700 °C–800 °C under open circuit voltage, shows that the maximum power density reached $207.94 \text{ mW cm}^{-2}$ at 800 °C (Fig. 17a). To obtain the FT cell performance using a ceramic interconnect film, a comparison between a

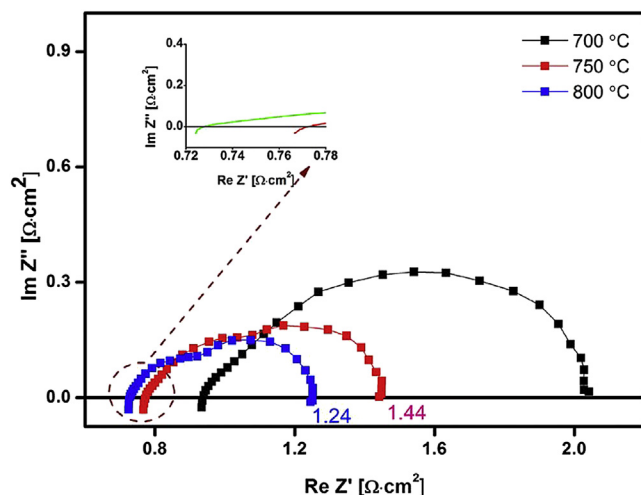


Fig. 16. Nyquist plot of the LCTM0.6 interconnect impedance under open circuit state between 700 °C and 800 °C.

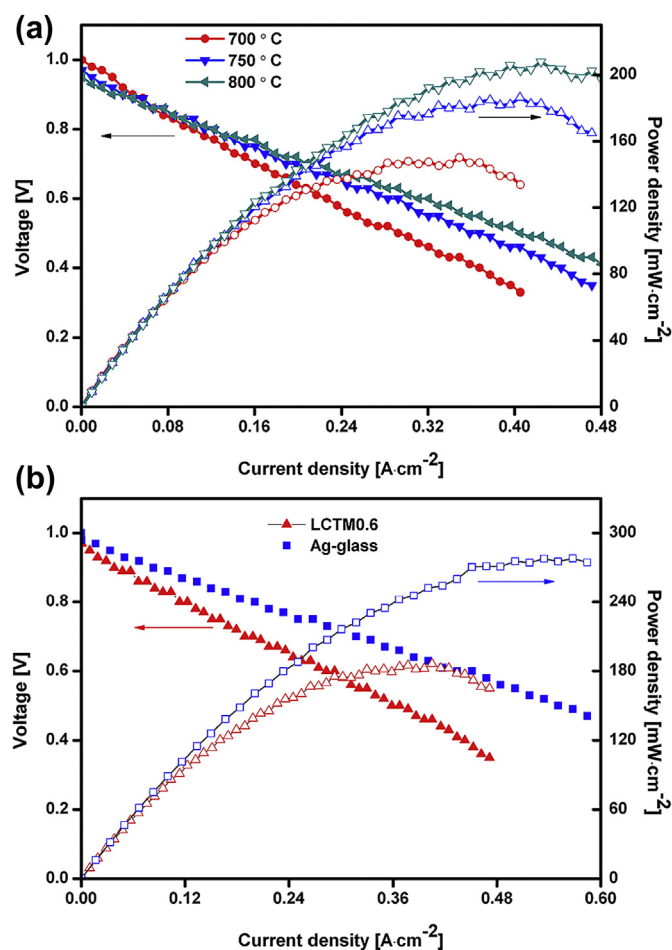


Fig. 17. (a) Polarization curves of FT-SOFC including LCTM0.6 interconnect under open circuit state between 700 °C and 800 °C, and (b) polarization curves of Ag-glass composite and LCTM0.6 interconnect at 750 °C.

cell coated with ceramic IC and a cell with Ag-glass composite IC was carried out (Fig. 17b).

The comparison was accomplished at 750 °C, because of the vaporization of Ag at higher temperatures [6]. It was observed that the maximum power density was reduced from approximately 280 mW cm^{-2} for Ag-glass composite IC to 186.3 mW cm^{-2} for LCTM0.6 using the ceramic IC. It confirms that almost 66% of power output can be achieved by LCTM0.6 IC layer.

Currently, an optimization work is in progress to further enhance the electrochemical performance by decreasing ohmic loss and consequently ASR value.

4. Conclusion

Dense nano-dimensional powders of $\text{La}_{0.4}\text{Ca}_{0.6}\text{Ti}_{(1-x)}\text{Mn}_x\text{O}_{3-\delta}$ ($x = 0.0, 0.2, 0.4, 0.6$) perovskite oxides were synthesized using an EDTA-citrate method. The influence of Mn doping on the crystal structure, microstructure, sintering shrinkage and temperature dependence of conductivity of the solid solution was investigated under both air and moist 5% H_2 –Ar atmospheres. Thermo-gravimetric analysis revealed the appropriate calcination temperature. All samples adopted the single perovskite phase after calcination at 950 °C for 5 h. Thermal expansion coefficients of the specimens were in close match with 8 mol% yttria-stabilized zirconia.

The highest conductivities of $\text{La}_{0.4}\text{Ca}_{0.6}\text{Ti}_{0.4}\text{Mn}_{0.6}\text{O}_{3-\delta}$ were $\sim 12.20 \text{ S cm}^{-1}$ and $\sim 2.70 \text{ S cm}^{-1}$ under oxidizing and reducing conditions, respectively. The anode support of an FT-SOFC was

successfully extruded and an LCTMx membrane was screen printed on the substrate and co-sintered. SEM micrograph confirmed a well-combined dense IC layer on the porous substrate. The maximum power density of the cell with ceramic IC was $207.94 \text{ mW cm}^{-2}$ when using H_2 as fuel and air as oxidant, and area specific resistance was calculated as $1.23 \Omega \text{ cm}^2$ at 800°C . The contributions of this study are:

- A screen-printing process is a simple approach to fabricate a dense ceramic layer on porous anode support;
- Co-sintering with other cell components is suggested as a significant replacement to reduce the number of fabrication steps;
- LCTMx ceramic perovskite consists of non-expensive, easily available precursors.

Stability, sinterability, linear thermal evolution of lattice parameters, and electrochemical properties make LCTMx a potential IC candidate for FT-SOFCs.

Acknowledgment

This work was supported by the National Research Foundation of Korea (NRF) grant funded by the Korea government (MEST) (no. 2012R1A2A2A03047613).

References

- [1] W.Z. Zhu, S.C. Deevi, *J. Mater. Sci. Eng. A* 348 (2003) 227–243.
- [2] K.-J. Yoon, C.N. Cramer, J.W. Stevenson, Olga A. Marina, *J. Power Sources* 195 (2010) 7587–7593.
- [3] K.-J. Yoon, C.N. Cramer, E.C. Thomsen, C.A. Coyle, G.W. Coffey, O.A. Marina, *J. Electrochem. Soc.* 157 (2010) B856–B861.
- [4] J.W. Fergus, *Solid State Ionics* 171 (2004) 1–15.
- [5] J.-H. Kim, R.-H. Song, K.-S. Song, S.-H. Hyun, D.-R. Shin, H. Yokokawa, *J. Power Sources* 122 (2003) 138–143.
- [6] B.-K. Park, J.-W. Lee, S.-B. Lee, T.-H. Lim, S.-J. Park, R.-H. Song, D.-R. Shin, *J. Power Sources* 213 (2012) 218–222.
- [7] S. Simner, J. Hardy, J. Stevenson, T. Armstrong, *J. Mat. Sci.* 34 (1999) 5721–5732.
- [8] O.P. Shrivastava, N. Kumar, I.B. Sharma, *J. Mater. Sci.* 27 (2) (2004) 121–126.
- [9] U. Balachandran, N.G. Error, *J. Mater. Sci.* 17 (1982) 1795–1800.
- [10] U. Balachandran, N.G. Error, *J. Solid State Chem.* 39 (1981) 351–359.
- [11] V. Vashook, L. Vasylechko, M. Knapp, H. Ullmann, U. Guth, *J. Alloys Compd.* 354 (2003) 13–23.
- [12] V. Vashook, L. Vasylechko, N. Trofimenko, M. Kuznecov, P. Otchik, J. Zosel, U. Guth, *J. Alloys Compd.* 419 (2006) 271–280.
- [13] B.-K. Park, J.-W. Lee, S.-B. Lee, T.-H. Lim, S.-J. Park, R.-H. Song, W.-B. Im, D.-R. Shin, *Int. J. Hydrogen Energy* 37 (2012) 4319–4327.
- [14] V.A. Kolotygin, E.V. Tsipis, A.I. Ivanov, Y.A. Fedotov, I.N. Burmistrov, D.A. Agarkov, V.V. Sinitsyn, S.I. Bredikhin, V.V. Kharton, *J. Solid State Electrochem.* 16 (2012) 2335–2348.
- [15] O.A. Marina, N.L. Canfield, J.W. Stevenson, *Solid State Ionics* 149 (2002) 21–28.
- [16] M.J. Escudero, J.T.S. Irvine, L. Daza, *J. Power Sources* 192 (2009) 43–50.
- [17] D.N. Miller, J.T.S. Irvine, *J. Power Sources* 196 (2011) 7323–7327.
- [18] Q.X. Fu, F. Tietz, D. Stover, *J. Electrochem. Soc.* 153 (4) (2006) 74–83.
- [19] A. Ovalle, J.C.R. Morales, J.C. Vázquez, D.M. López, J.T.S. Irvine, *Solid State Ionics* 177 (2006) 1997–2003.
- [20] M. Kobayashi, R. Katsuraya, S. Kurita, M. Yamaguchi, H. Satoh, N. Kamegashira, *J. Alloys Compd.* 408–412 (2006) 1173–1176.
- [21] H. Taguchi, M. Sonoda, M. Nagao, *J. Solid State Chem.* 26 (1996) 235.
- [22] R. Ran, Y. Guo, Y. Zheng, K. Wang, Z. Shao, *J. Alloys Compd.* 491 (2010) 271–277.
- [23] X. Huang, H. Zhao, W. Shen, W. Qiu, W. Wu, *J. Phys. Chem. Solids* 67 (2006) 2609–2613.
- [24] T. Bak, J. Nowotny, C.C. Sorrell, M.F. Zhou, *J. Mater. Sci. Mater. Electron.* 15 (2004) 635–644.
- [25] F.A. Kröger, *J. Appl. Crystallogr.* 8 (1975) 497–498.
- [26] U. Balachandran, B. Odekirk, N.G. Error, *J. Mater. Sci.* 17 (1982) 1656–1662.
- [27] Q.X. Fu, S.B. Mi, E. Wessel, F. Tietz, *J. Eur. Ceram. Soc.* 28 (2008) 811–820.
- [28] Y. Shen, M. Liu, T. He, S.P. Jiang, *J. Power Sources* 196 (2011) 8531–8538.
- [29] Y. Zhang, C. Xia, M. Ni, *Int. J. Hydrogen Energy* 37 (2012) 3392–3402.
- [30] F. Zhao, V. Virkar, *J. Power Sources* 141 (2005) 79–95.
- [31] M. Chen, B.-H. Kim, Q. Xu, B.-G. Ahn, D.-P. Huang, *J. Membr. Sci.* 360 (2010) 461–468.
- [32] S.B. Adler, B.T. Henderson, M.A. Wilson, D.M. Taylor, R.E. Richards, *Solid State Ionics* 134 (2000) 35–42.
- [33] C.-W. Chen, D.-S. Tsai, T.-Y. Jin, W.-H. Chung, C.-C. Chou, *Solid State Ionics* 179 (2008) 330–337.